



1 Long-term surface energy balance of the western Greenland ice sheet 2 and the role of large-scale circulation variability

3 Baojuan Huai¹, Michiel R. van den Broeke², Carleen H. Reijmer²

4 1. College of Geography and Environment, Shandong Normal University, Jinan, China

5 2. Institute for Marine and Atmospheric Research, Utrecht University, Utrecht, The Netherlands

6 **Abstract.** We present the surface energy balance (SEB) of the west Greenland ice
7 sheet (GrIS), using an energy balance model forced with hourly observations from
8 nine automatic weather stations (AWS) along two transects: the K-transect with seven
9 AWS in the southwest and the T-transect with two AWS in the northwest. Modeled
10 and observed surface temperatures for non-melting conditions agree well, with
11 RMSEs of 1.1-1.6 K, while reasonable agreement is found between modeled and
12 observed 10-day cumulative ice melt. Absorbed shortwave radiation (S_{net}) is the main
13 energy source for melting (M), followed by the sensible heat flux (Q_h). The multi-year
14 average seasonal cycle of SEB components show that S_{net} and M peak in July at all
15 AWS. The turbulent fluxes of sensible (Q_h) and latent heat (Q_l) decrease significantly
16 with elevation, and the latter becomes negative at higher elevations, partly offsetting
17 Q_h . Average June, July, August (JJA) albedo values are < 0.6 for stations below 1,000
18 m asl and > 0.7 for the higher stations. The near-surface climate variables and surface
19 energy fluxes from reanalysis products ERA-interim, ERA5 and the regional climate
20 model RACMO2.3 were compared to the AWS values. The newer ERA5 product
21 only significantly improves on ERA-interim for albedo. The regional model
22 RACMO2.3, which has higher resolution (5.5 km) and a dedicated snow/ice module,
23 unsurprisingly outperforms the re-analyses for (near-) surface climate variables, but
24 the reanalyses are indispensable to detect dependencies of west Greenland climate and
25 melt on large-scale circulation variability. We correlate ERA5 with the AWS data to
26 show a significant positive correlation of western GrIS summer surface temperature
27 and melt with the Greenland Blocking Index (GBI), and weaker and opposite
28 correlations with the North Atlantic Oscillation (NAO). This analysis may further help
29 to explain melting patterns in the western GrIS from the perspective of circulation
30 anomalies.

31 1 Introduction

32 In recent decades, the Greenland ice sheet (GrIS) has been a major contributor to
33 global sea-level rise, and is expected to remain so in the future (*Shepherd et al., 2019*),
34 raising worldwide concerns for coastal flooding and negative impacts on ecosystems
35 (*IPCC, 2019*). In-situ measurements provide crucial insights into the processes
36 causing temporal and spatial GrIS melt variability, notably how the various



37 components of the surface energy balance (SEB) contribute to snow and ice ablation.
38 Automatic Weather Stations (AWS) monitor the near-surface atmospheric conditions
39 on the ice sheet and -when equipped with radiation sensors- have proven to be
40 excellent tools to determine the SEB and therewith quantify melt energy. At present
41 there are >30 semi-permanent AWS installed on the GrIS. The largest GrIS AWS
42 network currently operational is the Programme for Monitoring of the Greenland Ice
43 Sheet (PROMICE; *Ahlstrøm et al., 2008; Van As et al., 2011*). PROMICE AWS are
44 mainly situated in the narrow and low-lying ablation zone, and are operated by the
45 Geological Survey of Denmark and Greenland (GEUS) in collaboration with the
46 National Space Institute at the Technical University of Denmark (Greenland Survey).
47 Other AWS networks are GC-Net, operated by the Cooperative Institute for Research
48 in Environmental Sciences (CIRES; *Steffen and Box., 1996, 2001*), and situated
49 mainly in the accumulation zone, and the K-Transect, a combined AWS-mass
50 balance-ice velocity stake network operated since 1990 by the Institute for Marine and
51 Atmospheric Research, Utrecht University (IMAU) (*Smeets et al., 2018*).

52 In recent decades, multiple observational studies described the local SEB on the
53 GrIS. *Hoch et al. (2007)* made year-round radiative flux observations at Summit, the
54 highest point on the GrIS. *Van den Broeke et al. (2008a, b)* and *Kuipers Munneke et al.*
55 *(2018)* used measurements from four AWSs to describe the SEB along the K-transect
56 in the southwestern GrIS. *Fausto et al (2016)* investigates two high melt episodes in
57 the southern GrIS in the summer of 2012 and quantified and ranked melt energy
58 sources through the melt season.

59 Until now, few studies addressed AWS- derived SEB and melt on the GrIS in
60 terms of regional circulation variability. Statistical analysis suggests that southern
61 GrIS climate responds strongly to atmospheric warming (*Hanna and Cappelen 2003*),
62 and that Greenland overall has been one of the fastest warming regions of the
63 Northern Hemisphere in the last 10~25 years (*Hanna et al., 2014*). These changes in
64 GrIS summer near surface air temperature are caused both by changes in the local
65 atmospheric heat balance and by changes in the large-scale atmospheric circulation
66 (*Van den Broeke et al., 2017; No ð and others, 2019*). *Rajewicz and Marshall (2014)*
67 state that "...circulation anomalies explain 38-49% of the summer air temperature and
68 melt extent variability in GrIS over the period 1948-2013." Greenland high pressure
69 blocking is a key feature of circulation variability in the western North Atlantic
70 (*Ballinger et al., 2018*). Strong Greenland blocking episodes have been linked to
71 exceptional surface melting of the western GrIS (*Hanna et al., 2014, Hanna et al.*
72 *2016*), and recently a Greenland Blocking Index (GBI) has been defined by *Fang*
73 *(2004)* and *Hanna et al. (2013, 2014, 2015)*. Another important regional mode of
74 large-scale atmospheric circulation variability is the North Atlantic Oscillation (NAO)
75 (*Hurrell et al., 2003; Van den Broeke et al., 2017*).

76 To study the dependency of regional west Greenland SEB and melt on
77 large-scale circulation variability we use data from two GrIS AWS transects, i.e. the
78 southwestern Kangerlussuaq (K-) transect and the northwestern Thule (T-) transect. In
79 addition, we use reanalysis (ERA5, ERA-Interim) data and output of a regional



80 atmospheric climate model (RACMO2.3) to obtain spatially continuous results. ERA5
81 is the latest reanalysis product from the European Centre for Medium-Range Weather
82 Forecasts (ECMWF; *Dee et al., 2011; Hersbach and Dee, 2016*), and replaces
83 ERA-Interim, considered to be the leading product over GrIS until now (*Albergel et*
84 *al., 2018; Bromwich et al., 2016*). However, so far little is known about the
85 performance of ERA5 over the GrIS. Because both the PROMICE and IMAU AWS
86 are not assimilated in ERA5, these data can be used to assess its quality and that of
87 regional climate models. Thus, we also include an evaluation of ERA5/RACMO2.3
88 SEB components over the western GrIS.

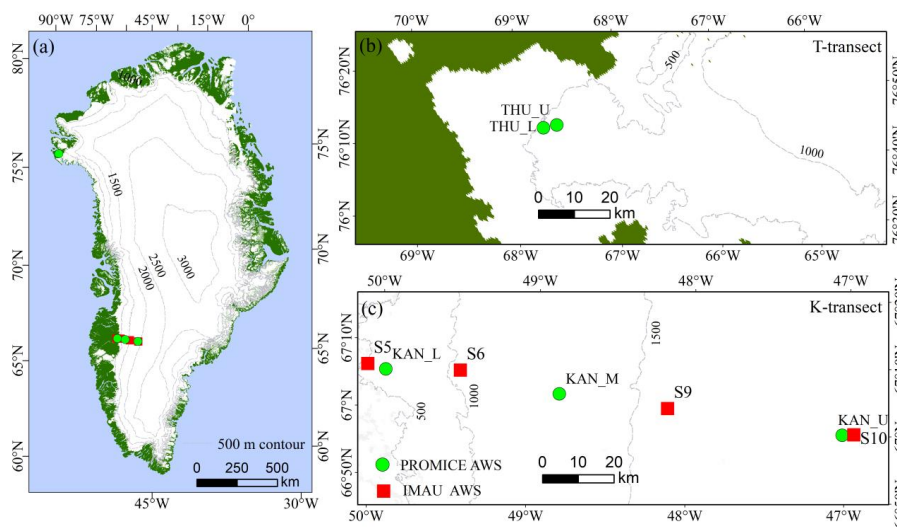
89 This paper is organized as follows. The AWS sites and data used to force the
90 SEB model are described in Section 2, followed by the SEB model description in
91 Section 3. The results Section 4 is split into three parts: we present the SEB results
92 along the two GrIS transects and we evaluate the near-surface climate and SEB in
93 ERA5 and RACMO2.3, after which we discuss their dependency on the large-scale
94 circulation indices GBI and NAO.

95

96 **2 Study sites, observational and model data**

97 **2.1 AWS transects**

98 To calculate the SEB and melt rate, we use data of all seven AWS along the
99 K-transect in the southwestern GrIS, i.e. four IMAU AWS (S5, S6, S9 and S10) and
100 three PROMICE AWS (KAN_L, KAN_M and KAN_U, Fig. 1c). We also use data of
101 the two PROMICE AWS located near Thule, dubbed the T-transect, in the
102 northwestern GrIS (THU_L and THU_U, Fig. 1b). The K-transect was initiated in the
103 summer of 1990 as part of the Greenland Ice Margin EXperiment (*GIMEX;*
104 *Oerlemans and Vugts 1993; Kuipers Munneke et al., 2018*) and originally represented
105 an array of three AWS (S10 was added later) and eight surface mass balance/ice
106 velocity sites. In 2008 and 2009, three more sites were added to the K-transect as part
107 of the PROMICE AWS network (*Van As et al., 2011; Fausto et al., 2012a*). The
108 topographic details as well as the observational period, climate characteristics and
109 AWS sensor specifications are listed in Tables 1 and 2.



110

111 **Fig 1.** The two GrIS AWS transects used in this study (a): blue represents ocean, green ice-free
 112 tundra and white glaciated areas and location of AWS sites. The transects are magnified in b) and
 113 c). Red squares are IMAU AWS and green circles PROMICE AWS. Grey dashed lines are 500 m
 114 elevation contours.

115

Table 1 AWS location, elevation and start of observations

Station	Latitude(N)	Longitude(W)	ELA(m a.s.l)	Start Date
S5	67.08	50.10	490	27/08/2003
S6	67.07	49.38	1020	01/01/2003
S9	67.05	48.22	1520	26/08/2003
S10	67.00	47.02	1850	17/08/2010
KAN_L	67.10	49.95	670	01/09/2008
KAN_M	67.07	48.84	1270	02/09/2008
KAN_U	67.00	47.03	1840	04/04/2009
THU_L	76.40	68.27	570	09/08/2010
THU_U	76.42	68.15	760	09/08/2010

116

Table 2 AWS sensor specifications

Sensors	PROMICE Type	IMAU Type	PROMICE Accuracy	IMAU Accuracy
Temperature	MP100H-4-1-03-00-10DIN	Vaisala HMP45C	< 0.1 K	0.4°C at -20°C
Air pressure	CS100-Setra model 278	Vaisala PTB101B	1.5 hPa	4 hPa
Wind speed	05103-5. R.M. Young	05103-L.R.M.Young	0.3 m s ⁻¹	0.3 m s ⁻¹
Wind direction	05103-5.R.M. Young	05103-L.R.M.Young	3 °	3 °



Humidity	HygroClip S3	Vaisala HMP45C	1.5 % RH/0.3 °C	2% for RH <90%
Radiation	Kipp Zonen CNR1 or CNR4	Kipp Zonen CNR1	10% of daily totals	10% of daily totals
Surface height	SR50A sonic ranger	SR50 sonic ranger	1 cm or $\pm 0.4\%$ *	0.01 m
	Ørum & Jensen NT1400 pressure transducer		2.5 cm*	

117 *PROMICE AWS pressure transducer sensor accuracy from Fausto et al. (2012)

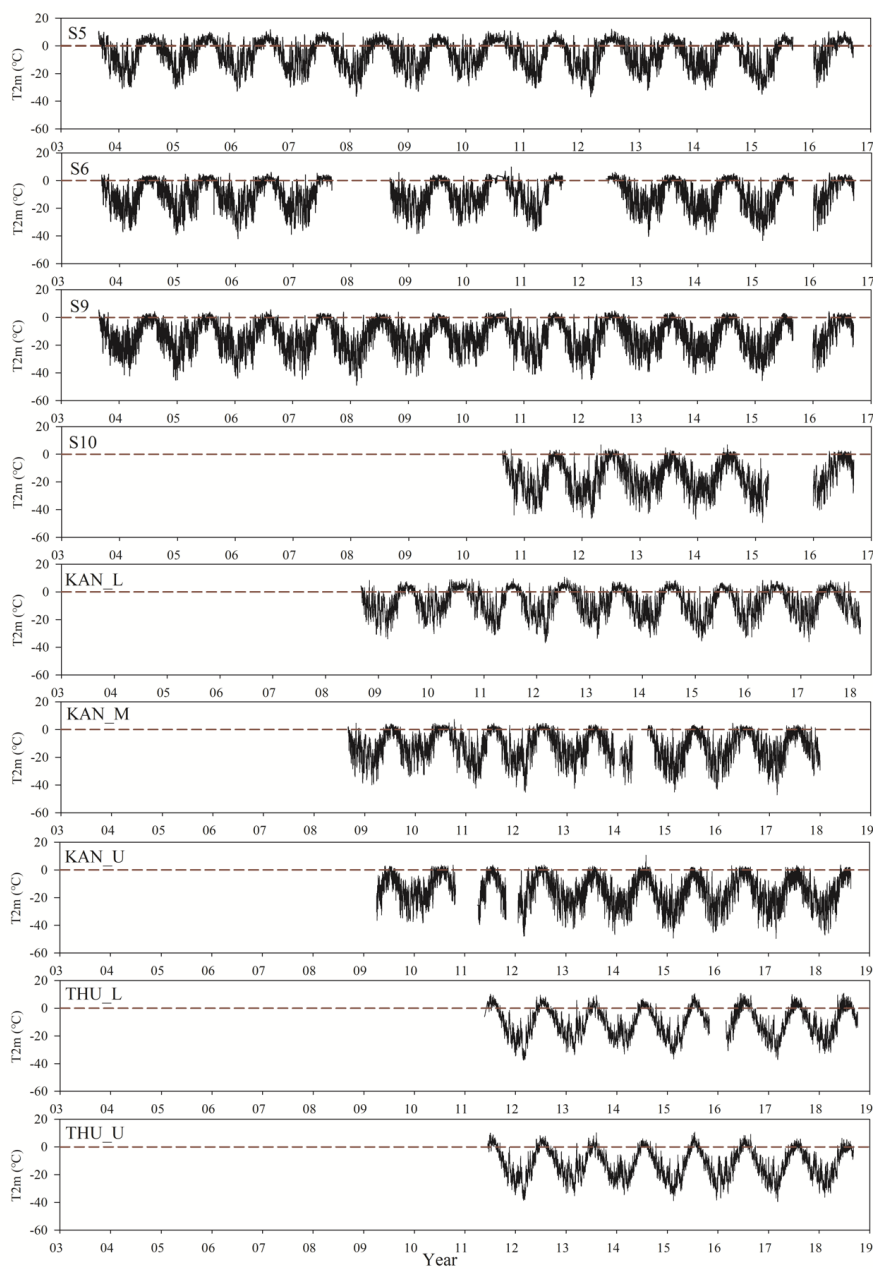
118 2.2 Data

119 2.2.1 AWS data and processing

120 Hourly average wind speed, incoming and reflected shortwave radiation,
 121 incoming and emitted longwave radiation, air temperature, relative humidity and air
 122 pressure are used to drive the SEB model. To illustrate the data time series at the nine
 123 AWS, Figure 2 shows the full temperature records, where temperature is recalculated
 124 to the reference height of 2 m using the SEB model. Note that S6 data gaps include
 125 large parts of 2008, 2010, 2012 and 2015, while the other AWS have generally more
 126 complete coverage.

127 Snow and ice height records cannot always be used directly to assess sensor
 128 height changes because of AWS design changes and/or settling of the structure. For
 129 PROMICE AWS, we use the results from a physically based method to remove
 130 air-pressure variability from the signal of the pressure transducer records (*Fausto et*
 131 *al., 2012b; Van As et al., 2011*). For details of S5, S6, S9 and S10 data biases,
 132 corrections, and data gap filling in case of sensor failure, we refer to *Smeets et al.*
 133 *(2018)*.

134 In the model evaluation using surface temperature, we use all-period data, while
 135 in the evaluation of melt using measured height changes, we use the period starting in
 136 2008 to maximize data overlap. For annual or multi-year averages of SEB
 137 components, we use complete years only (Table 3 and Table S1 and Figures 7, 8, 9
 138 and 10). Data points used in Figure 4 coincide with time series in Figure 2, while
 139 Figure 6 starts in 2008.



140

141

Fig 2. Time series of 2 m temperature (T2m) at the nine AWS sites used in this study

142

2.2.2 ERA5

143

144

The fourth-generation European Centre for Medium Range Weather Forecasts (ECMWF) Interim Reanalysis (*ERA-Interim, Dee et al., 2011*), available at a spatial



145 resolution of 0.75 ° and a 6-hourly time resolution, has been widely used over the GrIS
146 (*Bromwich et al., 2016, Albergel et al., 2018*). ERA-Interim is not continued beyond
147 August 2019, and is replaced by the follow-on product ERA5. The latter has a higher
148 spatial (31 km) and temporal (hourly) resolution (*ECMWF, 2018; Delhasse et al.,*
149 *2019*). Beside the higher time and horizontal resolution and updated physics package,
150 the main improvements for ERA5 compared to ERA-Interim are a higher number of
151 vertical levels, an improved 4D-VAR assimilation system and more data assimilated
152 (*ECMWF, 2018*). In addition to using ERA5 near-surface climate variables and SEB
153 components for evaluation, we also use ERA5 500 hPa geopotential height for the
154 GBI and NAO regression analysis.

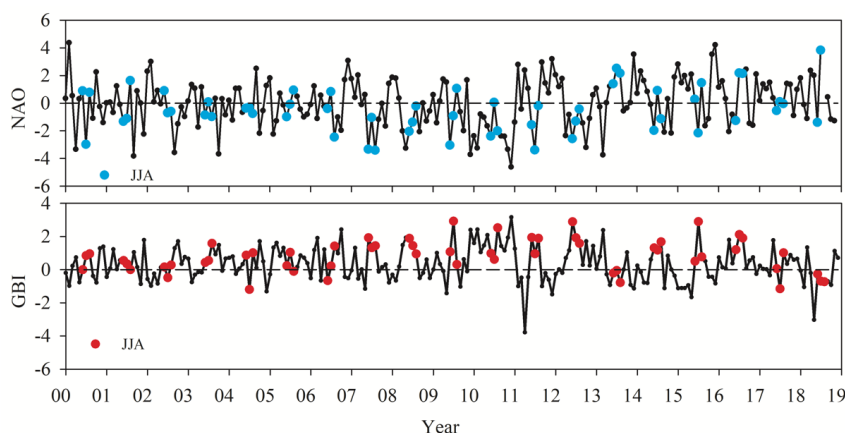
155 2.2.3 RACMO2.3

156 The Regional Atmospheric Climate Model (RACMO2) is developed and
157 maintained at the Royal Netherlands Meteorological Institute (KNMI) (*Van Meijgaard*
158 *et al., 2008*). The polar version of RACMO2 was developed at IMAU, to specifically
159 represent the SMB of polar ice sheets such as the GrIS (*Ettema et al., 2010*).
160 RACMO2.3 incorporates the dynamical core of the High-Resolution Limited Area
161 Model and the physics from the ECMWF Integrated Forecast System (*ECMWF-IFS,*
162 *2008; No ð et al., 2018*). We use output at 5.5 km horizontal spatial resolution of the
163 polar version of RACMO2.3 for the period 2003-2018 with a daily time resolution
164 (*No ð et al., 2018*) for evaluation and monthly 2 m temperature and melt flux data for
165 GBI and NAO correlation analysis presented in Section 2.2.4.

166 2.2.4 Monthly GBI and NAO index

167 The Greenland Blocking Index (GBI) represents the mean 500 hPa geopotential
168 height for the 60-80 °N, 20-80 °W region (*Hanna et al., 2014, 2015*), while the North
169 Atlantic Oscillation (NAO) index represents the normalized sea level pressure
170 difference between Iceland and the Azores (*Hurrell et al., 1995; Jones et al., 2003;*
171 *Hurrell et al., 2012*). The GBI and NAO-index time series are made available by the
172 US National Oceanographic and Atmospheric Administration (NOAA)'s Earth
173 System Research Laboratory Physical Sciences Division at: [http://www.esrl.noaa.gov/](http://www.esrl.noaa.gov/psd/data)
174 [psd/data](http://www.esrl.noaa.gov/psd/data) and are plotted in Figure 3, in which the blue and red dots represent June,
175 July and August (JJA) values. The two indices are not independent, with a correlation
176 coefficient between JJA NAO and GBI values for this period of -0.65, i.e. Greenland
177 blocking is associated with less zonally oriented large-scale flow over the North
178 Atlantic, as expected.

179



180

181 **Fig 3.** Time series of monthly average NAO and GBI indices where the blue and red dots are
 182 values for June, July, August (JJA)

183 **3 Surface energy balance model**

184 **3.1 Model description**

185 The Surface Energy Balance (SEB) model uses AWS data as input and solves for
 186 the surface temperature T_s at which the SEB is closed, i.e.:

187
$$M = S_{in} + S_{out} + L_{in} + L_{out} + Q_h + Q_l + G + Q_p \quad (1)$$

188 in which M is the energy used for melt ($M = 0$ when $T_s < 273.15K$), S_{in} and S_{out}
 189 are the observed incoming and reflected shortwave radiation fluxes, L_{in} and L_{out} are
 190 the observed incoming and calculated outgoing longwave radiation fluxes (assuming
 191 unit emissivity), Q_h and Q_l are the calculated sensible and latent turbulent heat fluxes,
 192 G is the surface value of the calculated sub-surface heat flux and Q_p is the heat flux
 193 supplied by rain. All fluxes are evaluated at the surface and fluxes towards the surface
 194 are defined positive. In this study, Q_p is neglected because no information on rainfall
 195 timing and rate is available. A previous study used precipitation data from the
 196 HIRHAM5 regional climate model bi-linearly interpolated to AWS locations, and
 197 reported that the rain heat flux on average contributed ~1% to the melt flux in summer
 198 at the southern GrIS sites QAS_L (Fausto et al., 2016).

199 Q_h and Q_l are estimated using the bulk aerodynamic approach with stability
 200 corrections based on Monin-Obukhov similarity theory (Van den Broeke et al., 2005;
 201 Smeets and Van den Broeke., 2008), using the stability functions of Holtslag and de
 202 Bruin., 1988. The expressions used to calculate Q_h and Q_l are as follows:

203
$$Q_h = \rho_a c_p u_* \theta_* = \rho_a c_p C_H u (\theta - \theta_s) \quad (2)$$

204
$$Q_l = \rho_a L_v u_* q_* = \rho_a L_v C_E u (q - q_s) \quad (3)$$



205 Where u_* , θ_* and q_* are the turbulent scales for momentum, heat and moisture, c_p
206 is the specific heat capacity of air at constant pressure, ρ_a is air density, L_v is the latent
207 heat of sublimation and C_H and C_E are bulk exchange coefficients for heat and
208 moisture, respectively. The SEB model uses the measured atmospheric temperature,
209 wind speed and humidity at the AWS sensor level together with the (iteratively
210 estimated) surface temperature, assuming zero wind speed and saturated humidity
211 values at the surface. The surface roughness length for momentum (z_0) varies strongly
212 in time and space in the ablation zone of GrIS, and is often set to different constant
213 values for snow and ice surfaces (Smeets and van den Broeke., 2008; Brock et al.,
214 2006), while the values for heat (z_h) and moisture (z_q) are estimated following the
215 expressions due to Andreas et al. (1987). Based on previous work with observations
216 from both the lower and upper measurement levels to compute a temporally evolving
217 z_0 value at sites S5 and S6 (Smeets and van den Broeke., 2008), a z_0 value of $1.3 \cdot 10^{-3}$
218 m is chosen for S5, S6, and KAN_L when ice is at the surface, and $1.3 \cdot 10^{-4}$ m when
219 snow covers the surface at these AWS sites. At S9, S10, KAN_M and KAN_U, we
220 use a constant z_0 value of $1 \cdot 10^{-3}$ m for ice as the annual cycle is much smaller at
221 these stations (Van den Broeke et al., 2005), while $1 \cdot 10^{-4}$ m is used for snow. At
222 THU_L and THU_U, we use ice values of $1.2 \cdot 10^{-3}$ m and $1 \cdot 10^{-3}$ m and snow values
223 of $1.3 \cdot 10^{-4}$ m and $1 \cdot 10^{-4}$ m for THU_U, respectively. The z_0 values of all the stations
224 are listed in Tables 3.

225 **Table 3** The surface roughness length for momentum (z_0) at the nine AWS sites

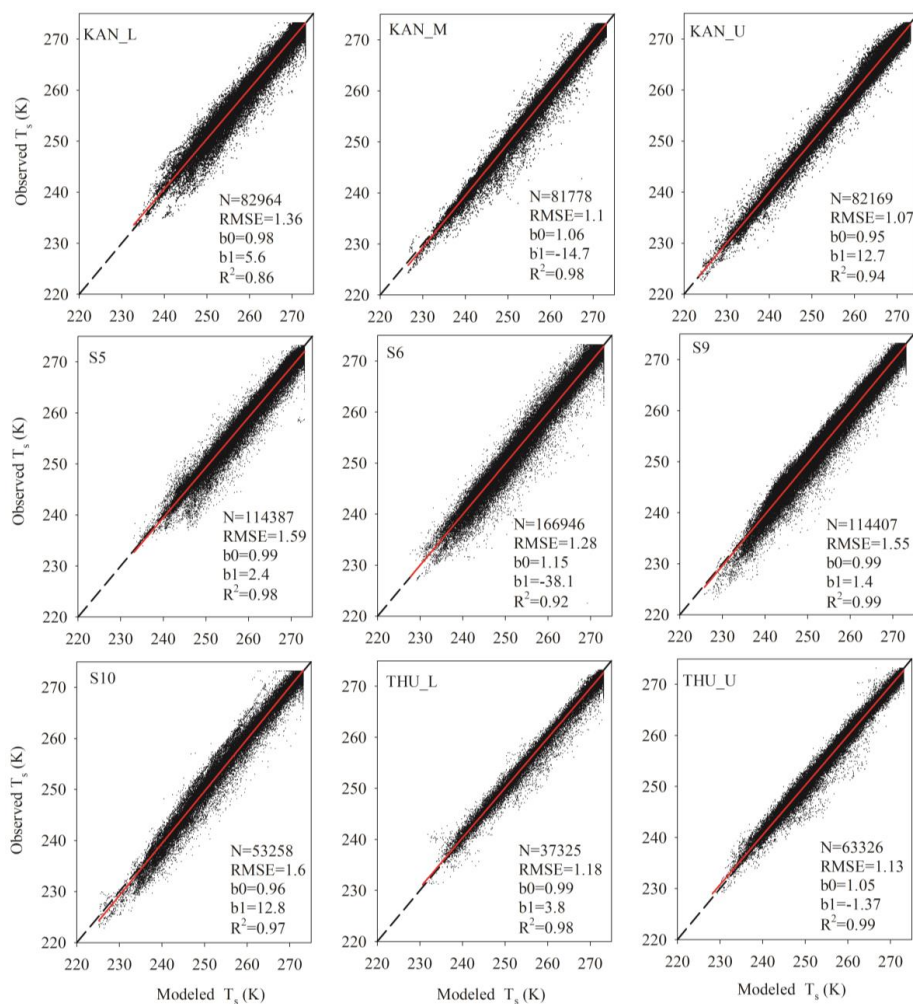
Station	Ice z_0	Snow z_0
S5	$1.3 \cdot 10^{-3}$	$1.3 \cdot 10^{-4}$
S6	$1.3 \cdot 10^{-3}$	$1.3 \cdot 10^{-4}$
S9	$1.0 \cdot 10^{-3}$	$1.0 \cdot 10^{-4}$
S10	$1.0 \cdot 10^{-3}$	$1.0 \cdot 10^{-4}$
KAN_L	$1.3 \cdot 10^{-3}$	$1.3 \cdot 10^{-4}$
KAN_M	$1.0 \cdot 10^{-3}$	$1.0 \cdot 10^{-4}$
KAN_U	$1.0 \cdot 10^{-3}$	$1.0 \cdot 10^{-4}$
THU_L	$1.2 \cdot 10^{-3}$	$1.3 \cdot 10^{-4}$
THU_U	$1.0 \cdot 10^{-3}$	$1.0 \cdot 10^{-4}$

226 The G calculation uses the vertical temperature distribution in the near surface
227 snow layers, as calculated in the sub-surface part of the SEB model, based on the
228 SOMARS model (Simulation Of glacier surface Mass balance And Related
229 Sub-surface processes, Greuell and Konzelman, 1994) with skin layer formulation
230 (Van den Broeke et al., 2011) in which penetration of shortwave radiation is neglected
231 (Van den Broeke et al., 2011). For a more detailed description of the model and recent
232 applications, we refer to Reijmer (2002, 2008), Van den Broeke (2004, 2008a,b, 2011),
233 Kuipers Munneke (2009, 2012, 2018).



234 **3.2 SEB model evaluation**

235 The calculation proceeds as follows. The SEB components L_{out} , Q_h , Q_l and Q_g
236 are expressed in terms of surface temperature, and the SEB model then iteratively
237 searches for the value of T_s at which the SEB is closed. When T_s exceeds the melting
238 point, it is set to 273.15 K and the remaining energy is used for melting. The
239 root-mean-square-error (RMSE) between hourly modelled and observed T_s , the latter
240 derived from L_{out} assuming unit emissivity, is used to evaluate model performance at
241 the nine AWS locations in Figure 4. The RMSE varies from 1.1 K at KAN_U to 1.6 K
242 at S10. The results show that at KAN_M (RMSE=1.1), KAN_U (RMSE=1.1),
243 THU_L (RMSE=1.2) and THU_U (RMSE = 1.1) the model performs better than at S5
244 (RMSE=1.6) and S10 (RMSE =1.6). Overall, at the 9 AWS, observed and modeled
245 surface temperatures agree largely to within the observational uncertainty.



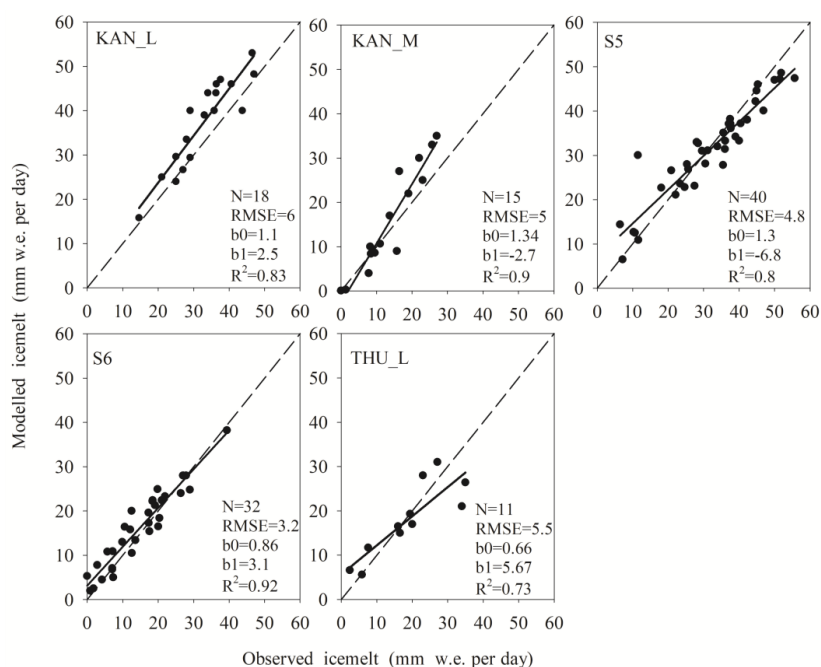
246



247 **Fig 4.** Modeled and observed hourly surface temperature T_s for the nine AWS. The dashed black
 248 line represents the 1:1 line and the red solid line the linear regression. Statistics show the number
 249 of data points (N), root-mean-squared-error (RMSE), regression slope (b_0) and intercept (b_1), and
 250 coefficient of determination (R^2).

251 During melt, when the surface temperature is fixed at 273.15 K, T_s can no longer
 252 be used for evaluation, and we assess model performance by comparing observed and
 253 modeled ice melt, assuming the density of ice to be known. This does not work for S9,
 254 S10 and THU_U which are situated above the equilibrium line, and hence on firn with
 255 unknown density. A 10-day period is chosen, to reduce the measurement noise so that
 256 a meaningful comparison is possible (Van den Broeke *et al.*, 2008b). The corrected
 257 pressure transducer melt data collected by PROMICE AWS and SR50A sonic ranger
 258 collected by IMAU AWS are converted to mass changes (mm w.e.) by assuming an
 259 ice density of 910 kg/m^3 . Figure 5 shows reasonable agreement between modeled and
 260 observed 10-day ice melt for KAN_L, KAN_M, S5, S6 and THU_L.

261 At S5 and S6, Van den Broeke *et al.* (2008b) and Kuipers Munneke *et al.* (2018)
 262 compared annual ice ablation versus stake observations. They found that although
 263 results agreed within the model and measurement uncertainty, the relative differences
 264 for individual years could be substantial, up to 20%. Here, differences for individual
 265 10-day periods of up to 46% are found, but the average difference is small, 6%.



266
 267 **Fig 5.** Average 10-day modeled and observed ice melt (expressed in mm w.e. per day) for the
 268 five AWS situated in the ablation zone, assuming an ice density of 910 kg/m^3 . The dashed line is
 269 the 1:1 line and the solid line the linear regression line. Statistics show the number of data points



270 (N), root-mean-squared-error (RMSE), regression slope (b_0) and intercept (b_1), and coefficient of
271 determination (R^2).

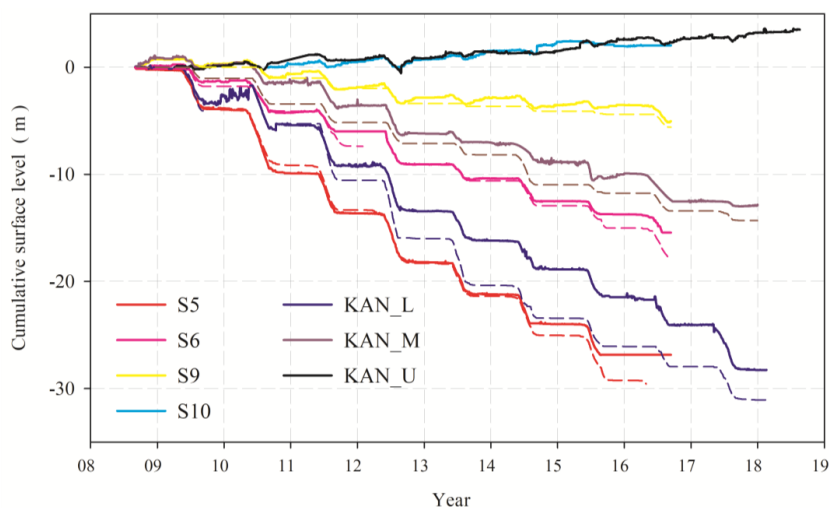
272 Apart from model uncertainties, there are various possible explanations for the
273 differences. *Fausto et al (2016)* show that in the lower ablation area in the southern
274 GrIS (QAS_L), the average rain energy flux in JJA averaged 1% of the total melt
275 energy flux but can reach 5 - 9 % during high melt episodes. *Van den Broeke et al*
276 *(2008b)* calculated the impact of radiation penetration on melt at S5, and showed that
277 melt energy was only slightly smaller than in the case without radiation penetration.
278 Based on this we expect that neglecting subsurface radiation penetration has little
279 effect on the total cumulative melt flux.

280 **4 Results and Discussion**

281 **4.1 SEB and comparison of the two transects**

282 4.1.1 Surface height change

283 The measured surface height change and modelled cumulative ice melt for the
284 seven K-transect stations (S5, S6, S9, S10 and KAN_L, KAN_M, KAN_U) are
285 shown in Figure 6. From 2008 to 2017, the ablation at S5 and KAN_L reached nearly
286 30 m of ice while for the stations above the equilibrium line (~1500 m a.s.l.) the total
287 accumulation was about 4 m of firn. At site S5 (490 m a.s.l.) the modeled ice melt and
288 measured surface height change agree well, even in winter, indicating that there is
289 little snow accumulation in winter at this site, as supported by visual observations. At
290 site KAN_L (670 m a.s.l.), there are obvious accumulation events in the winter in
291 2009 and 2011, and modeled ice melt is generally larger than observed. The strongest
292 melt occurred in summer 2012, contributing to the largest annual ice-sheet mass loss
293 on record (*Khan et al., 2015*), followed by a return to more average conditions in
294 2013 (*Nghiem et al., 2012; Kuipers Munneke et al., 2018*). Overall, modelled and
295 observed total height change agree typically within 10%.



296

297 **Fig 6.** Measured height changes (solid lines) and modelled ice melt (dashed line) at the seven
 298 K-transect AWS.

299 4.1.2 SEB components

300 Table 4 shows that average summer (June, July, August; JJA) net shortwave
 301 radiation S_{net} provides most (67% at S5 to 95% at S9) of the energy used for heating
 302 or melting the surface along both transects (Van As *et al.*, 2012; Van den Broeke *et al.*,
 303 2008b; 2009). On average, S_{net} is largest at KAN_L (125 W m^{-2}), and smallest at S10
 304 (65 W m^{-2}). For the T-transect, average S_{net} decreases from 84 W m^{-2} at THU_L to 74
 305 W m^{-2} at THU_U. The generally lower values in the northwestern GrIS can be
 306 explained by the difference in latitude but also by a smaller value of the shortwave
 307 transmissivity (0.63 at KAN_L vs. 0.53 at THU_L in summer, using top-of-
 308 -atmosphere radiation data from ERA5), probably owing to more frequent and thicker
 309 clouds along the T-transect (cloud cover 0.51 at KAN_L vs. 0.56 at THU_L in
 310 summer, using cloud cover estimates from PROMICE AWS based on L_{in} and air
 311 temperature). Along the K-transect, JJA L_{in} ranges between 250 and 285 W m^{-2} , while
 312 L_{out} varies between 298 and 314 W m^{-2} . Along the T-transect, L_{in} is 273 to 279 W m^{-2}
 313 and L_{out} 309 to 312 W m^{-2} . The reduced longwave heat loss confirms higher
 314 cloudiness in the northwest GrIS, in agreement with Van As *et al.* (2012).

315 **Table 4** Energy fluxes (W m^{-2}) averaged over June, July, August (JJA) at the nine AWS
 316 locations, SEB values of L_{out} , Q_h , Q_l , G and M are derived from the SEB model while S_{in} , S_{out} and
 317 L_{in} are from observations.

Flux	S5	KAN_L	S6	KAN_M	S9	KAN_U	S10	THU_L	THU_U
S_{in}	249	265	267	256	294	300	295	231	249
S_{out}	-136	-140	-154	-158	-211	-234	-230	-147	-176
S_{net}	113	125	113	114	92	66	65	84	74



L_{in}	285	283	265	263	255	250	253	279	273
L_{out}	-314	-314	-311	-308	-306	-298	-301	-312	-309
L_{net}	-29	-29	-45	-44	-51	-48	-48	-33	-36
R_{net}	84	96	68	70	42	18	17	51	38
Q_h	45	28	18	8	5	7	3	21	11
Q_l	3	-3	-0.4	-10	-4	-12	-6	-11	-6
G	-10	1	-8	-6	-0.2	7	7	1	1
M	-122	-119	-77	-62	-42	-20	-20	-61	-44

318 S_{net} clearly is the main energy source for heating and melt at the ice sheet in
 319 summer, followed by the sensible heat flux. Q_h is larger than Q_l for the low elevation
 320 stations, with a JJA average of 45, 28 and 18 $W m^{-2}$ for S5, KAN_L and S6,
 321 respectively, indicating significant contributions to the melt energy. At higher
 322 elevations, Q_h becomes small and Q_l significantly negative (sublimation), with a JJA
 323 average of -4, -12 and -6 $W m^{-2}$ for S9, KAN_U and S10, respectively. As a result,
 324 above the equilibrium line, the two turbulent fluxes tend to (partly) cancel. However,
 325 summertime S_{net} and L_{net} are also negatively correlated, indicating that net radiation
 326 R_{net} is always substantially smaller than S_{net} . This means that, when compared to R_{net} ,
 327 Q_h does provide a significant contribution to summer melt and surface heating energy,
 328 ranging from 12% at S9 to 37% at S5.

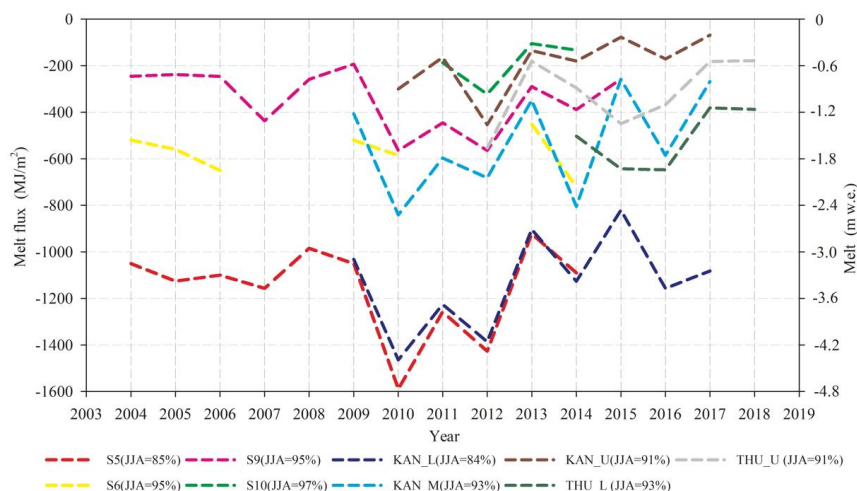
329 The important role of Q_h in the GrIS SEB becomes even more evident if we look
 330 at annual mean SEB components (Table S1 in the Supplementary Materials). In winter,
 331 Q_h becomes the main source of surface warming. In the absence of absorbed
 332 shortwave radiation, wintertime Q_h balances a large part of L_{net} so that annual mean
 333 Q_h is relatively large and annual R_{net} at S5, KAN_L, S6 and KAN_M becomes small
 334 with values of 10, 14, 23 and 6 $W m^{-2}$, respectively, and even becomes negative for
 335 the higher stations S9, KAN_U and S10. Sites with negative annual mean R_{net} are very
 336 rare at the Earth's surface, and require an efficient local atmospheric heat source,
 337 which over the GrIS is provided by the mixing of relatively warm air aloft to the ice
 338 sheet surface by katabatic winds, resulting in large Q_h and large negative L_{out} . Annual
 339 average values of Q_h are as high as 32 $W m^{-2}$ for S5 decreasing to 6 $W m^{-2}$ at S10, 20
 340 $W m^{-2}$ for THU_L and 16 $W m^{-2}$ for THU_U. The annual mean latent heat flux Q_l
 341 varies between -1 $W m^{-2}$ and -6 $W m^{-2}$.

342 Figure 7 shows the interannual variability of the annual melt energy and the
 343 corresponding melt water equivalent. The legend lists the percentage contribution
 344 from JJA melt for each station. Significant inter-annual variability is present in the
 345 annual melt energy; the standard deviation of the annual melt as a fraction of the
 346 average value for stations with > 5 years of data ranges from 119 $MJ m^{-2}$ (61% of the
 347 mean) at KAN_U to 209 $MJ m^{-2}$ (39%) at KAN_M. For most locations, 2010 and/or
 348 2012 were the strongest melt years, with the highest ablation of 4.8 m w. e. per year
 349 being reached at S5 in 2010. Only S5 (85%) and KAN_L (84%) experience
 350 significant (>10%) non-summer melt, otherwise JJA melt energy contributes more



351 than 90% to the annual total melt energy. No significant trend is present in any of
 352 these time series, because they are all relatively short and exhibit large year-to-year
 353 variability.

354 Melt (M) at the K- transect AWS sites is significantly higher than at the T-
 355 transect: average annual magnitude of M for THU_L is 512 MJ m^{-2} compared to 1160
 356 MJ m^{-2} and 1133 MJ m^{-2} for S5 and KAN_L, respectively. Obviously, this can be
 357 partly explained by differences in absorbed short-wave radiation caused by the
 358 different latitudes of the two transects and the lower temperatures further north,
 359 resulting in a shorter ablation season. In the discussion section, we address the
 360 potential role of atmospheric circulation.



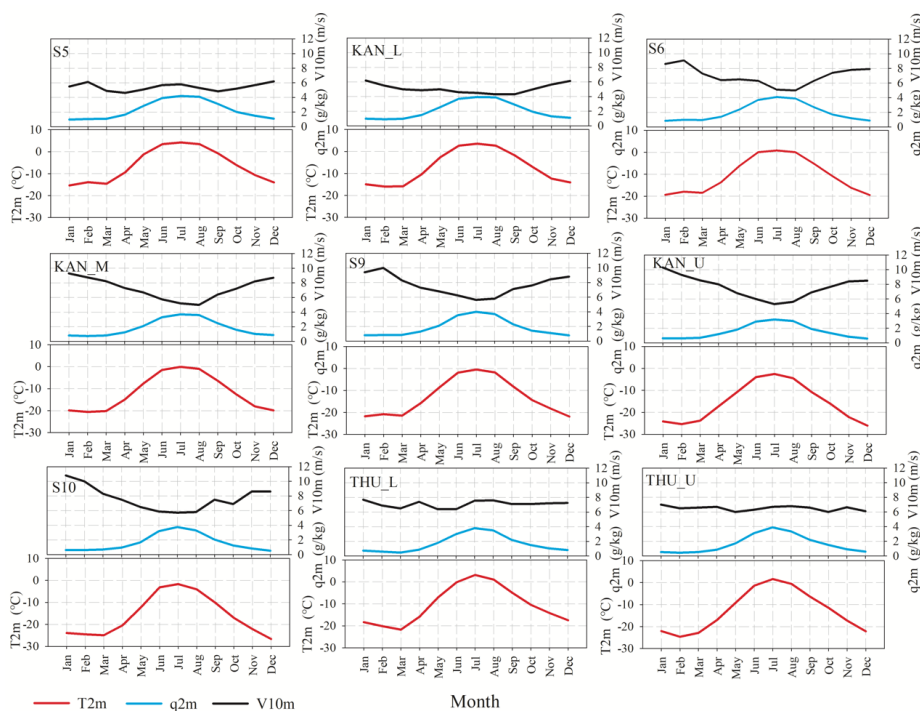
361

362 **Fig 7.** Annual melt energy (2003-2018) at the nine AWS sites and JJA melt energy percentage of
 363 the annual total. Dashed line is the annual melt energy (MJ m^{-2}) and the right y-axis represents the
 364 approximate melt water equivalent (m w.e.).

365 Figure 8 presents the multi-year average seasonal cycle of 2 m temperature, 2 m
 366 specific humidity and wind speed at 10 m at the nine AWS sites while Figure 9 shows
 367 the multi-year average seasonal cycle of SEB components. Temperature and melt peak
 368 in July for all sites. Average JJA T_{2m} decreases with increasing latitude from $3.0 \text{ }^\circ\text{C}$ at
 369 KAN_L to $1.4 \text{ }^\circ\text{C}$ at THU_L. The JJA elevational temperature gradient along the
 370 K-transect is obvious with $3.7 \text{ }^\circ\text{C}$ at S5 decreasing to $-3.0 \text{ }^\circ\text{C}$ at S10. Specific
 371 humidity largely follows temperature. Wind speeds are katabatic in nature and
 372 generally stronger in winter than in summer for the K-transect AWS sites. The
 373 exception is S5 where wind speed shows a double peak because of persistent surface
 374 melting in summer, i.e. like winter generating a situation with a colder surface and
 375 warmer overlying air, generating persistent glacier winds. These higher wind speeds
 376 enable the highest values for Q_h for S5 as the strong wind shear enhances turbulent
 377 mixing in summer, in spite of the strongly stable stratification (Figure 9). The average
 378 summertime wind speeds at the T- transect AWS (7.2 m/s at THU_L and 6.6 m/s at



379 THU_U are generally higher than at similar elevations along the K- transect (5.5 m/s
 380 at KAN_M and 5.8 m/s at S10), and show a less well developed seasonal cycle,
 381 possible owing to stronger synoptic forcing and higher cloud cover which limits
 382 surface cooling to drive katabatic flow.



383

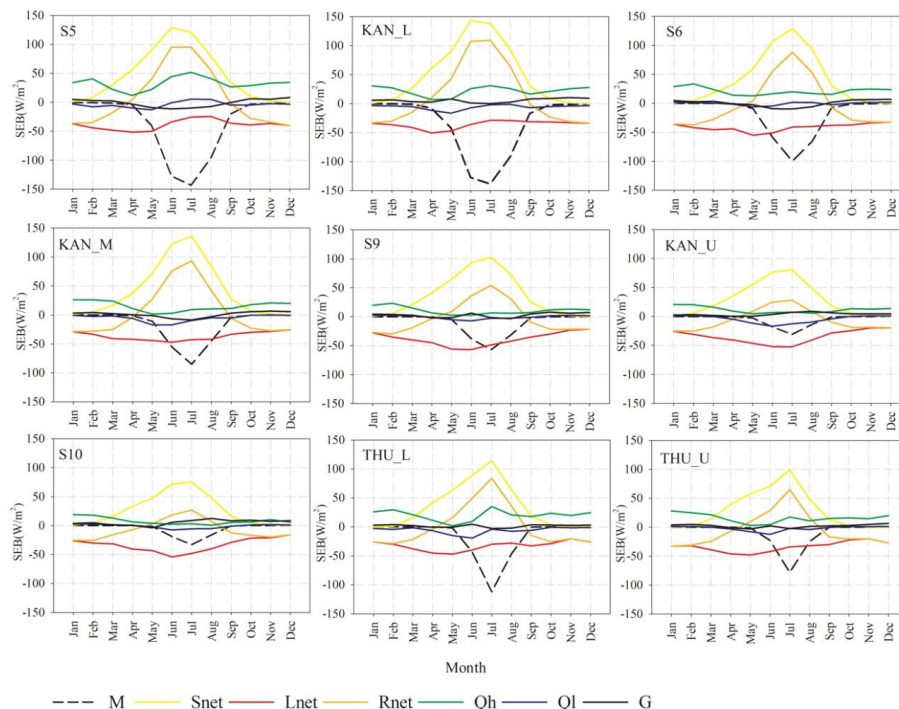
384 **Fig 8.** Multi-year average seasonal cycle based on monthly means of 2 m temperature (red, T_{2m}),
 385 specific humidity (blue, q_{2m}) calculated from relative humidity and wind speed at 10 m (black,
 386 V_{10m}).

387 Figure 9 shows the seasonal cycle of SEB components. M peaks in July at all
 388 sites, mainly following R_{net} . But July melt differences with June are small at the lower
 389 stations S5 and KAN_L where low wintertime accumulation means that the albedo
 390 assumes the lower ice value early in the melt season, meaning that the main energy
 391 source for melt, S_{net} , peaks at the end of June around the summer solstice. Melting
 392 occurs as early as March and lasts until September at S5 and KAN_L, while S6 and
 393 KAN_M also experience some melting in September. At THU_L and THU_U the
 394 sharp peak in S_{net} illustrates the shorter summer melt period.

395 For the lower AWS sites (S5, KAN_L, S6, KAN_M and THU_L), the shape of
 396 the L_{net} curve is relatively flat or even shows a maximum in summer. This is again a
 397 signature of persistent surface melt at these lower sites, with the surface temperature
 398 limited to a constant 273.15 K, limiting longwave heat loss from the surface
 399 irrespective of L_{in} (Van den Broeke, et al., 2011). For the higher AWS sites (S9,



400 KAN_U, S10 and THU_U) a minimum is reached later in spring, because the surface
 401 is not yet melting and can still increase its temperature (and therewith L_{out}) in
 402 response to increased absorption of solar radiation (S_{net}), at least for part of the day.



403

404 **Fig 9.** Multi-year average seasonal cycle based on monthly means of SEB components.

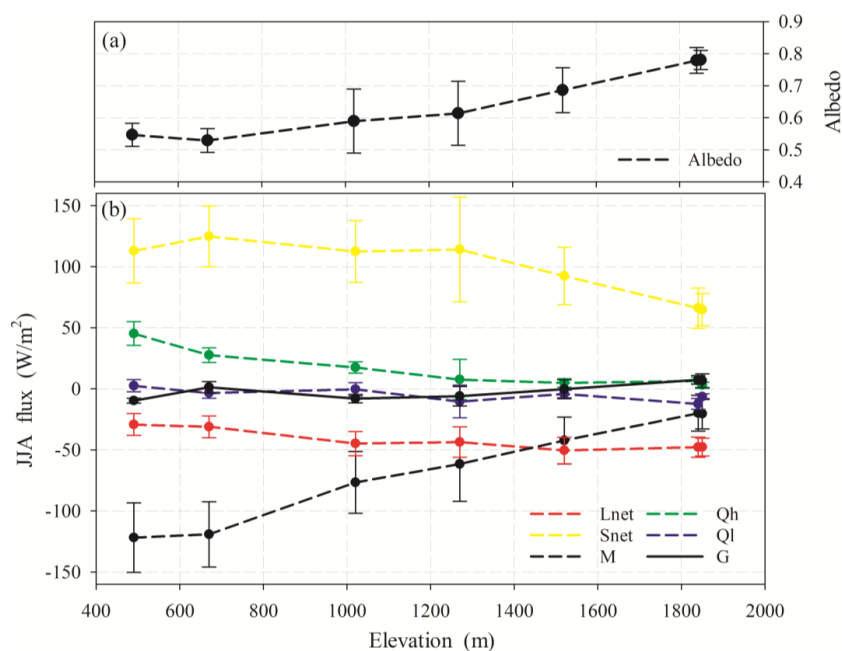
405 The shapes of the seasonal Q_h cycle at different AWS sites differ significantly.
 406 All stations show a maximum in winter, reflecting that Q_h is the most efficient SEB
 407 component to balance L_{net} ; the turbulent cooling of the air over the sloping ice sheet
 408 surface results in katabatic winds that effectively mix the near surface air. In summer,
 409 a second maximum occurs at S5, KAN_L and THU_L. These low-lying stations are
 410 reached by relatively warm air in summer as shown in Figure 8, creating a strong
 411 temperature gradient with the melting ice sheet, resulting in shallow katabatic flow
 412 (glacier winds) and hence a large Q_h that contributes significantly to melt (*Van den*
 413 *Broeke, 1996; Van den Broeke et al., 2005*). At S5, KAN_L and THU_L, JJA Q_h
 414 averages 45, 28, and 21 $W m^{-2}$, respectively, at least double that of the more elevated
 415 and hence colder inland sites (KAN_M: 8 $W m^{-2}$ and KAN_U: 7 $W m^{-2}$). The latent
 416 heat flux is generally small and negative, again with the exception of the lowest
 417 stations where the persistent melting limits saturation specific humidity at the surface,
 418 enabling condensation, making Q_l a small heat source for melting. The strongest
 419 sublimation rates are found in spring at the higher stations, when the sun heats the
 420 surface without it reaching the melting point, enhancing the moisture gradient from
 421 the surface to the near-surface air. Seasonal changes in G are small in comparison



422 with the other SEB components.

423 4.1.3 Variations of surface energy flux with elevation (K-transect)

424 The seven AWS along the K-transect enable the construction of robust JJA
425 SEB-elevation profiles (Fig 10). The average albedo in JJA (June, July and August),
426 calculated by dividing the total cumulative JJA values of S_{out} and S_{in} , of S5, KAN_L
427 and S6 all were under 0.6, at KAN_M and S9 values were between 0.6 ~ 0.7, and at
428 KAN_U and S10 all values were higher than 0.7. Figure 10 shows that the magnitude
429 of the melt energy M decreases significantly as the elevation increases, from 122 $W m^{-2}$
430 m^{-2} at S5 to 20 $W m^{-2}$ at S10, in line with S_{net} which changes from 125 $W m^{-2}$ to 65
431 $W m^{-2}$ and Q_h which decreases from 45 to 3 $W m^{-2}$, merely reflecting lower air
432 temperatures and a shorter melt season at the inland sites. Q_l decreases from near zero
433 to being significantly negative ($-12 W m^{-2}$) at S10, reflecting significant surface
434 cooling by sublimation. Net longwave radiation also becomes a more dominant
435 surface heat sink at higher elevations. These profiles are valuable for the evaluation of
436 reanalysis products and (regional) climate models that are used to simulate and predict
437 melting at the surface of the GrIS. For several climate products this is done in the next
438 section.



439

440 **Fig 10.** Mean June, July, August (JJA) SEB components and albedo versus elevation along the
441 K-transect. Error bars indicate standard deviation in the multi-year annual mean.

442 4.2 SEB evaluation in ERA5, ERA-Interim and RACMO2.3



443 We use the results presented in the previous section to evaluate T_{2m} , albedo,
444 radiation fluxes, Q_h and Q_l in ERA5, ERA-interim, and RACMO2.3p2, the latter
445 forced at the lateral boundaries by ERA-interim during 2003-2018. We compute
446 model output at the AWS locations using an average distance-weighted interpolation
447 method using the four nearest grid points. Evaluation of KAN_L, KAN_M, KAN_U,
448 THU_L and THU_U are included in the Supplementary Materials, and the evaluation
449 of S5, S6, S9 and S10 can be found in *Noð et al., (2018)*. Tables S2-S6 (In the
450 Supplementary Materials) show the root mean square error (RMSE), the mean bias
451 (MB) and the correlation coefficient (R) based on linear regressions on daily
452 observations of the PROMICE AWS. KAN_L observations of T_{2m} are well
453 represented in each of the models, but the differences with SEB components are
454 significant. Although ERA-5 better represents the observations than ERA-interim, the
455 improvement is not statistically significant (*Delhasse et al., 2019*). For Q_h and Q_l ,
456 RACMO2.3 provides the highest correlations. For THU_U (Table S3), RACMO2.3
457 shows high correlation coefficients for shortwave fluxes and 2 m temperature, and Q_h
458 and Q_l are also relatively well represented with correlation coefficients between 0.8
459 and 0.7, higher than the ERA-reanalyses. For albedo, ERA5 performs significantly
460 better than ERA-interim both at KAN_L and THU_U. It turns out that ERA5 does not
461 significantly improve on ERA-Interim for near-surface climate and SEB in west
462 Greenland, apart from albedo. RACMO2.3 outperforms the reanalyses both for 2 m
463 temperature and SEB components, with results similar to *Noð et al., (2018)*.

464 4.3 Discussion

465 To better understand the processes driving intra-seasonal and inter-annual SEB
466 variability in west Greenland, we combine the SEB results presented above with
467 indices of two dominant regional circulation patterns: the Greenland Blocking Index
468 (GBI, *Hanna et al., 2015*) and the North Atlantic Oscillation index (NAO, *Hurrell et*
469 *al., 1995; Jones et al., 2003*).

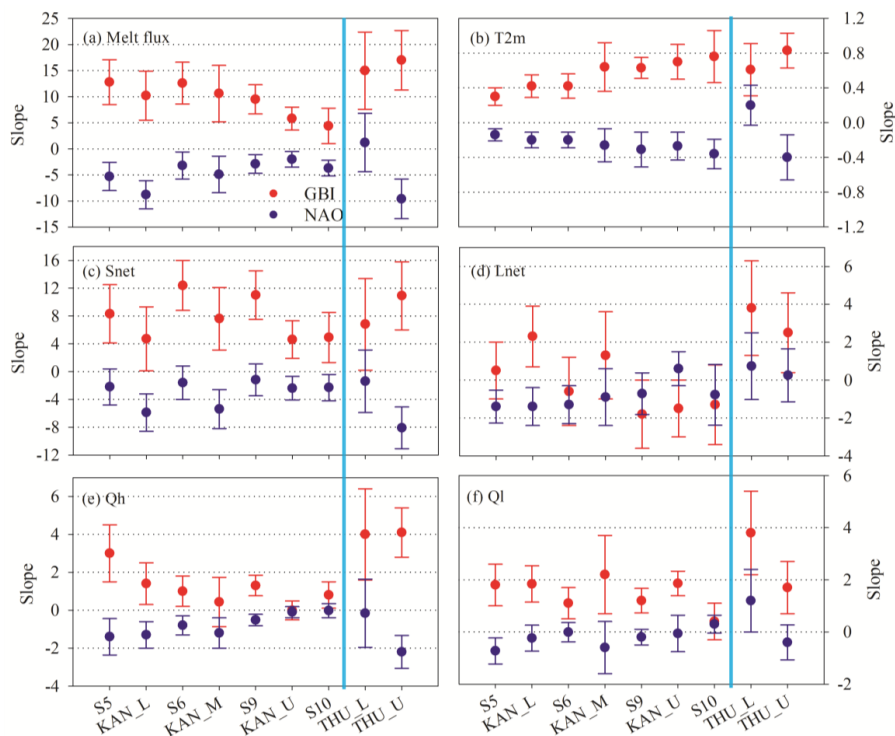
470 Figure 11 presents the linear regression slope values of NAO and GBI with
471 monthly mean AWS JJA SEB components and 2 m temperatures, with units $W m^{-2}$ or
472 K per one standard deviation change in GBI (σ_{GBI}) and NAO (σ_{NAO}). The error bars
473 indicate the uncertainty in the regression slope, which generally shows stations along
474 the T-transect having a higher uncertainty than along the K-transect, mainly caused by
475 the shorter time series in combination with large interannual variability. The
476 associated Pearson correlation coefficients (R) are presented in the Supplementary
477 Materials. For instance, Figure S1 shows that significant positive correlations between
478 JJA AWS melt fluxes, T_{2m} and the GBI are found for all AWS, whereas correlations
479 with NAO are weaker and generally negative (Figure S1a, b). For individual SEB
480 components S_{net} , L_{net} , Q_h and Q_l , correlations reach significance for some but not all
481 stations, but again are generally stronger for GBI than for NAO (Figure. S1 c-f).

482 In Figure 11 several interesting features can be identified. Starting with GBI (red
483 symbols), we find significantly positive dependencies between JJA AWS melt fluxes



484 and GBI for all AWS (Fig. 11a). Along the K-transect, the dependency decreases from
 485 a maximum of $13 \text{ W m}^{-2}/\sigma_{\text{GBI}}$ at S5 to $\sim 5 \text{ W m}^{-2}/\sigma_{\text{GBI}}$ at S10 and KAN_U. The
 486 dependencies of the individual SEB components along the K-transect are such that the
 487 increase in S_{net} (Fig. 11c) explains most (40-100%) of this melt increase, indicative of
 488 clearsky conditions during episodes of large positive GBI, in agreement with previous
 489 work (Hofer and others, 2018). Smaller contributions to the melt energy are made by
 490 Q_{h} (Fig. 11e) and Q_{l} (Fig. 11f), the latter becoming significant because of the limiting
 491 effect of surface melt on the surface temperature and hence its (saturated) specific
 492 humidity, decreasing the sublimation potential (i.e. making Q_{l} less negative). L_{net} (Fig.
 493 11d) contributes positively for the low-lying stations, again owing to the maximized
 494 surface temperature during melt, limiting L_{out} , and negatively for the higher stations, a
 495 result of enhanced surface cooling under clearsky, non-melting conditions. Surface
 496 melt also modulates the 2 m temperature response (Fig. 11b), with a muted response
 497 for the lower stations where melt is semi-permanent, and larger values at the higher
 498 stations, where melt is intermittent.

499 Albeit with larger uncertainties, consistently high melt sensitivities to variations
 500 in GBI of $>15 \text{ W m}^{-2}/\sigma_{\text{GBI}}$ are found at THU_L and THU_U. Also here, the largest
 501 contribution is made by S_{net} , but we find significant and approximately equal
 502 contributions from L_{net} , Q_{h} and Q_{l} . This suggests that in the northwest, high melt
 503 under high GBI conditions is associated with high temperatures and cloudiness.



504



505 **Fig 11.** AWS regression slope of JJA average SEB components and 2 m temperature (T2m) with
506 GBI (red dots) and NAO index (blue dots). Y axis are scaled with one standard deviation change
507 in GBI/NAO circulation index to show (a) the melt flux change from SEB model in W
508 $m^{-2}/\sigma_{GBI,NAO}$, (b) 2m temperature change from station in $Kelvin/\sigma_{GBI,NAO}$, (c) S_{net} change from
509 station in $W m^{-2}/\sigma_{GBI,NAO}$, (d) L_{net} change from station in $W m^{-2}/\sigma_{GBI,NAO}$, (e) Q_h change from
510 SEB model in $W m^{-2}/\sigma_{GBI,NAO}$ and (f) Q_l change from SEB model in $W m^{-2}/\sigma_{GBI,NAO}$. Error
511 bars indicate standard error in the multi-year JJA mean.

512 To better understand this spatially different response of western GrIS climate and
513 melt to GBI, Fig. 12 shows maps of the JJA GBI dependency for temperature (Fig.12a)
514 and melt (Fig. 12c) for Greenland and its immediate surroundings from RACMO2,
515 and Fig. 13a shows the regional 500 hPa height anomaly from ERA5. In the latter
516 figure we use ERA5 since the RACMO2 domain does not cover the whole of the
517 Arctic region. Both Figures 12 and 13 are based on data for the period 2000-2018 (19
518 years, 57 summer months). Figure S2 in the Supplementary Materials shows the
519 correlation coefficient of 2 m temperature and melt flux of RACMO2.3 with the JJA
520 GBI (Fig. S2a, S2c). Figure S2a shows R values for JJA 2 m temperature and GBI of
521 0.4-0.6 over the southwestern GrIS, very similar to the AWS results.

522 Figs. 12a, c confirm that the 2 m temperature/melt response to GBI are dominant
523 in west Greenland and weaker towards the east. The maps also confirm the observed
524 increasing/decreasing temperature/melt response with elevation in Figs. 11a, b under
525 high GBI conditions along the K-transect in the southwestern GrIS, and the enhanced
526 sensitivity in the northwest (Figs.12e and f show the enlarged images for melt). Fig.
527 13 shows that the large-scale circulation anomalies for high GBI conditions are very
528 different for the southwestern and northwestern GrIS: the maximum positive anomaly
529 is centered over the K-transect in the southwest, with the largest correlation
530 coefficient R (Fig. S3 in the Supplementary Materials) causing clearsky conditions
531 and a weak or absent circulation anomaly, which explains the dominant contribution
532 of S_{net} to the melt energy (Hofer *et al.*, 2017). In the northwest, a significant
533 circulation anomaly from the south and west means advection of warm and humid air,
534 resulting in higher temperatures and enhanced cloudiness, which explains the more
535 important contributions made to the melt anomaly by L_{net} , Q_h and Q_l (Noð *et al.*,
536 2019).

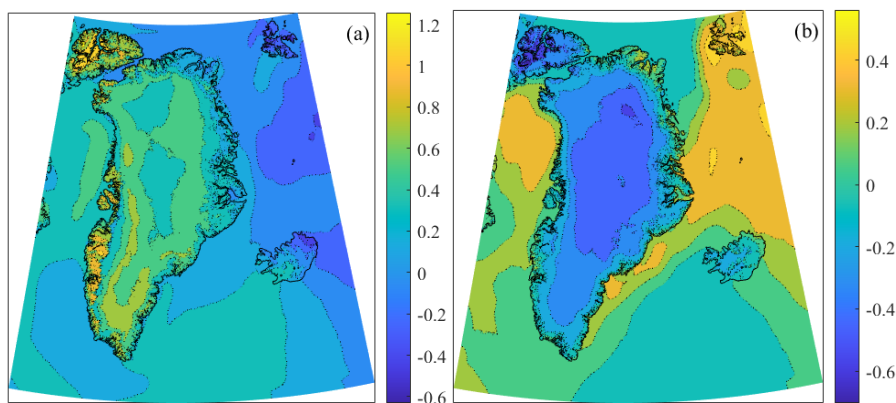
537 Since 2007, the GBI has been predominantly positive in summer (Figure 3), with
538 the exception of low-melt summers 2013 and 2018, and the strongest positive
539 anomalies in the strong melt summers 2012 and 2015 (Hanna *et al.*, 2016). High
540 summer GBI episodes are clearly linked to exceptional GrIS melt years (Hanna *et al.*,
541 2014), but Hanna *et al.*, (2013) our results highlight the complexity of the response to
542 summer GBI. Young-Kwon Lim *et al* (2016) show that in general, high pressure
543 blocking primarily impacts the western areas of the GrIS via advective temperature
544 increases. Rimbu and Lohmann., (2011) also found strong correlations between winter
545 temperatures across southwestern GrIS and high blocking activity in the GrIS,
546 whereas Hanna *et al.*, (2013) show that temperatures in Tasiilaq (southeast Greenland)

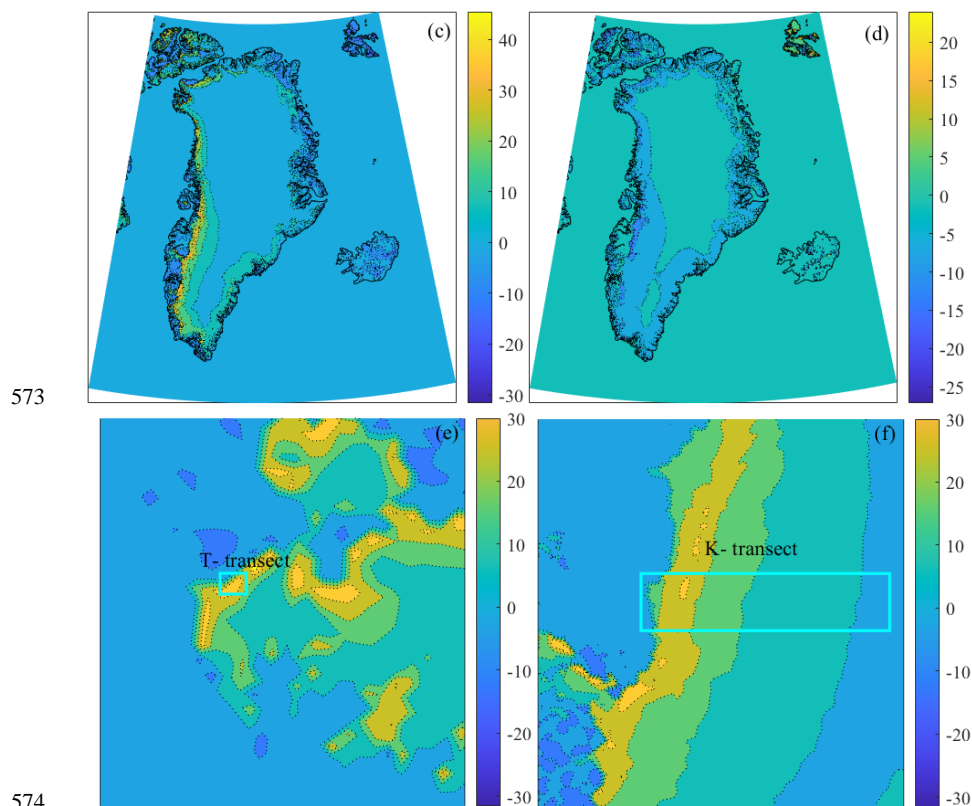


547 do not show significant correlations with GBI. Here we confirmed and discussed these
548 different responses.

549 Dependencies of summer AWS melt and 2 m temperatures with NAO are
550 negative and generally weaker (Fig. 11, blue dots), implying a weaker influence of the
551 NAO on western GrIS near-surface climate and melt compared to the GBI. Fig. 13b
552 confirms a weaker and less organized impact of NAO on the large-scale circulation in
553 west Greenland, with two centres of action in the area of the Icelandic Low in
554 southeast Greenland, and a secondary centre over the Arctic. *Hanna et al., (2015)*
555 noted that the more local geographic nature of the GBI means that it correlates more
556 directly with Greenland climate than the NAO index, and our results support this.
557 Several studies identified a link between anomalously high air temperatures over the
558 GrIS during negative NAO phases (*Hanna and Cappelen, 2003; Chylek et al., 2004*).
559 A negative NAO index (high air surface pressures in the North Atlantic) is often
560 accompanied by anticyclonic ridging in the GrIS region (*Rajewicz et al., 2014*). Our
561 results suggest that both GBI and NAO affect the southern GrIS, this part of the ice
562 sheet being wetter during NAO positive phases, while drier when GBI is positive.
563 *Davini et al (2012)* noted that the geographical dependence of GrIS climate on the
564 NAO shifted eastward, which is consistent with an increase in GBI. Given the large
565 natural, interannual variability, it remains difficult at present to exactly partition the
566 contributions of atmospheric circulation variability and Arctic warming to intensive
567 melting in the western GrIS. Our regression analysis may further help to explain the
568 melting pattern of the western GrIS from the perspective of circulation anomalies
569 (*Hanna and Cappelen 2003; Overland and Wang, 2010; Overland et al., 2012*). Also
570 note in Fig.12 how Svalbard temperature and melt show opposite responses to GBI
571 compared to west Greenland (*Young-Kwon Lim et al., 2016*).

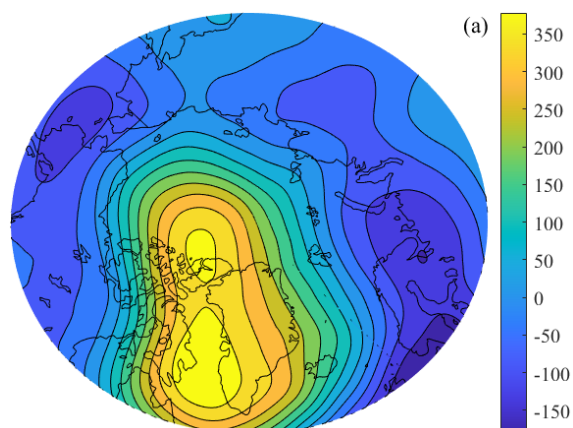
572

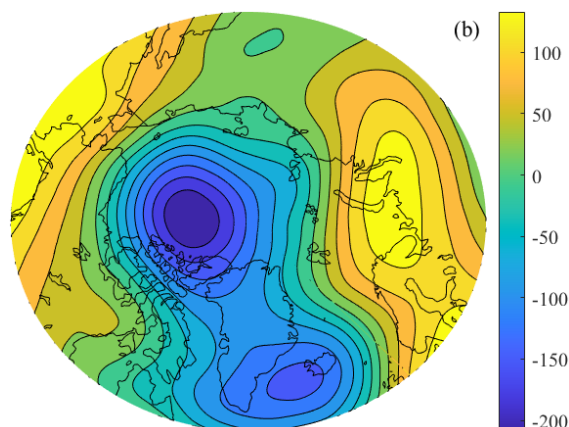




575 Fig 12. Regression slope of 2000–2018 JJA average 2 m temperature (T2m) from RACMO2.3
576 with (a) GBI and (b) NAO, melt flux from RACMO2.3 with (c) GBI and (d) NAO index.
577 Regression slope maps are scaled to show the 2m temperature change from RACMO2.3 in Kelvin
578 and melt flux change in $W m^{-2}$ for a one standard deviation change in GBI/NAO circulation index.
579 (e) and (f) are enlarged slope value image for T-transect and K-transect of JJA average melt flux
580 from RACMO2.3 with GBI. Black solid lines are Land-Sea Mask.

581





582

583 **Fig 13.** Regression fields slope of 2000~2018 JJA 500hpa geopotential height from ERA5
584 regressed with GBI (a) and NAO (b) index. Slope maps are scaled to show the 500hpa
585 geopotential height change from ERA5 in geopotential metres change in gpm for a one standard
586 deviation change in GBI (a) and NAO (b) circulation index.

587 5 Summary and conclusions

588 In this study, we forced a surface energy balance (SEB) model with data from
589 nine automatic weather stations (AWS) situated in the southwestern (seven) and
590 northwestern (two) Greenland ice sheet (GrIS). Absorbed shortwave radiation (S_{net}) is
591 the main energy source for melting (M), followed by the sensible heat flux (Q_h). The
592 multi-year average seasonal cycle of SEB components show that S_{net} and M all peak
593 in July, but that June is almost a similar strong melt month for the lowest stations. As
594 the length of the melt season and average albedo in JJA decrease with elevation, so
595 does melt; stations below 1,000 m asl show albedo values < 0.6 , while the higher
596 stations have > 0.7 . Q_h and the latent heat flux (Q_l) also decrease significantly with
597 elevation, and the latter becomes negative at higher elevations, partly offsetting Q_h as
598 a surface heat source.

599 We used the AWS-derived near-surface climate variables and SEB components to
600 evaluate the performance of two ECMWF reanalysis products (ERA5 and
601 ERA-Interim) as a regional climate model RACMO2.3. Only for albedo does the
602 newer ERA5 product significantly improve on ERA-Interim. The regional climate
603 model RACMO2.3 has higher resolution (5.5 km) and a dedicated snow/ice module,
604 and unsurprisingly outperforms the re-analyses.

605 From the decade-long observational time series, we inferred significant
606 inter-annual variability in melt energy and SEB components, hiding any significant
607 long-term trend. We report a strong positive correlation of the Greenland Blocking
608 Index (GBI) with western GrIS melt and 2m temperature, and weaker and negative
609 correlations with time series of summertime North Atlantic Oscillation (NAO) index.



610 **Supplementary Materials**

611 The following supporting information is available as part of this article:

612 Figure S1. AWS correlations of JJA average SEB components and 2 m temperature (T2m) with
613 GBI (red dots) and NAO index (blue dots).

614 Figure S2. Correlation fields of 2000~2018 JJA average 2 m temperature (T2m) from RACMO2.3
615 with (a) GBI and (b) NAO, melt flux from RACMO2.3 with (c) GBI and (d) NAO index.

616 Figure S3. Regression fields of 2000~2018 JJA 500hpa geopotential height regressed with GBI (a)
617 and NAO (b) index. The color bars show the correlation coefficient R.

618 Table S1 Annual surface energy fluxes (W m^{-2}) at the nine AWS locations, SEB values of L_{out} ,
619 Q_{h} , Q_{l} , G and M are derived from the SEB model while S_{in} , S_{out} and L_{in} are from observations.

620 Table S2 Root Mean Squared Error (RMSE), mean bias (MB) and correlation coefficient (R)
621 between daily AWS observations and ERA-Interim (EI), ERA5 (E5), RACMO2.3 (RAC) at
622 KAN_L

623 Table S3 Root Mean Squared Error (RMSE), mean bias (MB) and correlation coefficient (R)
624 between daily AWS observations and ERA-Interim (EI), ERA5 (E5), RACMO2.3 (RAC) at
625 KAN_M

626 Table S4 Root Mean Squared Error (RMSE), mean bias (MB) and correlation coefficient (R)
627 between daily AWS observations and ERA-Interim (EI), ERA5 (E5), RACMO2.3 (RAC) at
628 KAN_U

629 Table S5 Root Mean Squared Error (RMSE), mean bias (MB) and correlation coefficient (R)
630 between daily AWS observations and ERA-Interim (EI), ERA5 (E5), RACMO2.3 (RAC) at
631 THU_L

632 Table S6 Root Mean Squared Error (RMSE), mean bias (MB) and correlation coefficient (R)
633 between daily AWS observations and ERA-Interim (EI), ERA5 (E5), RACMO2.3 (RAC) at
634 THU_U

635 **Data availability.** The micrometeorological observations are available from the Programme for
636 Monitoring of the Greenland Ice Sheet (PROMICE) at <http://promice.org/DataDownload.html>,
637 and the ERA-Interim and ERA5 re-analyses are available from the ECMWF at
638 <https://www.ecmwf.int/en/forecasts/datasets/reanalysis-datasets>. All the results are available
639 through an email request to the authors.

640 **Author contributions.** MRB provided the topic and idea, BJH, MRB and CHR coordinated
641 the study and carried out the analysis; BJH and MRB drafted the paper, CHR edited the paper. All
642 authors contributed to the analysis, discussion and interpretation of the results.

643 **Competing interests.** The authors declare that they have no conflict of interest.

644 **Acknowledgements**



645 This work was funded by the Natural Science Foundation of China (41701059),
646 the Postdoctoral Science Foundation of China (40411594) and the Project for Outstanding Youth
647 Innovation Team in the Universities of Shandong Province (2019KJH011). The authors gratefully
648 acknowledge support from the Institute of Tibetan Plateau and Polar Meteorology, and data
649 availability from the Programme for Monitoring of the Greenland Ice Sheet (PROMICE) and the
650 ERA-Interim and ERA5 re-analyses projects of the ECMWF. The authors thank Brice Noël
651 (Utrecht University) for RACMO2 data support, Robert Fausto (GEUS) and Paul Smeets (Utrecht
652 University) for PROMICE and K-transect AWS technical information, and SEB model technical
653 support from Peter Kuipers Munneke, Maurice van Tiggelen and Constantijn Jakobs (all Utrecht
654 University).

655 **References**

- 656 Ahlstrøm, A.P. and PROMICE project team: A new programme for monitoring the mass loss of
657 the Greenland ice sheet. *Geological Survey of Denmark and Greenland Bulletin* 15, 61-64, 2008.
- 658 Albergel, C., Dutra, E., Munier, S., Calvet, J. C., Muñoz-Sabater, J., De Rosnay, P., and Balsamo,
659 G.: ERA-5 and ERA-Interim driven ISBA land surface model simulations: Which one performs
660 better? *Hydrology and Earth System Sciences*, 22, 3515-3532, [https://doi.org/10.5194/hess-22-](https://doi.org/10.5194/hess-22-3515-2018)
661 [3515-2018](https://doi.org/10.5194/hess-22-3515-2018), 2018.
- 662 Andreas, E.: A theory for the scalar roughness and the scalar transfer coefficients over snow and
663 sea ice, *Bound. Lay. Meteorol.*, 38, 159-184, 1987.
- 664 Ballinger, T.J., E. Hanna, R.J. Hall, J. Miller, M.H. Ribergaard, J.L. Høyer.: Greenland coastal air
665 temperatures linked to Baffin Bay and Greenland Sea ice conditions during autumn through
666 regional blocking patterns. *Clim. Dyn.*, 50, 83-100, 2018.
- 667 Brock, B.W., Willis, I. C., and Shaw, M. J.: Measurement and parameterization of aerodynamic
668 roughness length variations at Haut Glacier d'Arolla, Switzerland. *J. Glaciol.* 52, 281-297. doi:
669 [10.3189/172756506781828746](https://doi.org/10.3189/172756506781828746), 2006.
- 670 Bromwich, D. H., Wilson, A. B., Bai, L. S., Moore, G. W., and Bauer, P.: A comparison of the
671 regional Arctic System Reanalysis and the global ERA-Interim Reanalysis for the Arctic,
672 *Quarterly Journal of the Royal Meteorological Society*, 142, 644-658, [https://doi.org/10.1002/](https://doi.org/10.1002/qj.2527)
673 [qj.2527](https://doi.org/10.1002/qj.2527), 2016.
- 674 Chylek, P., J. E. Box, and G. Lesins.: Global warming and the Greenland ice sheet, *Clim. Change*,
675 63, 201-221, 2004.
- 676 Davini, P., C. Cagnazzo, R. Neale, J. Tribbia.: Coupling between Greenland blocking and the
677 North Atlantic Oscillation pattern. *Geophys. Res. Lett.* 39, L14701, 2012.
- 678 Dee, D. P., Uppala, S. M., Simmons, A. J., Berrisford, P., Poli, P., Kobayashi, S., Andrae, U.,
679 Balmaseda, M. A., Balsamo, G., Bauer, 35 P., Bechtold, P., Beljaars, A. C., van de Berg, L.,
680 Bidlot, J., Bormann, N., Delsol, C., Dragani, R., Fuentes, M., Geer, A. J., Haimberger, L., Healy,
681 S. B., Hersbach, H., Høm, E. V., Isaksen, L., Källberg, P., Köhler, M., Matricardi, M., McNally,
682 A. P., Monge-Sanz, B. M., Morcrette, J. J., Park, B. K., Peubey, C., de Rosnay, P., Tavolato, C.,
683 Thépaut, J. N., and Vitart, F.: The ERA-Interim reanalysis: Configuration and performance of the
684 data assimilation system, *Quarterly Journal of the Royal Meteorological Society*, 137, 553-597,
685 <https://doi.org/10.1002/qj.828>, 2011.
- 686 Delhasse, A., Christoph Kittel, Charles Amory, Stefan Hofer, and Xavier Fettweis, Brief



- 687 communication: Interest of a regional climate model against ERA5 to simulate the near-surface
688 climate of the Greenland ice sheet. *The Cryosphere Discuss.*, <https://doi.org/10.5194/tc-2019-96>,
689 2019.
- 690 ECMWF: What are the changes from ERA-Interim to ERA5? <https://confluence.ecmwf.int/pages/viewpage.action?pageId=74764925>, 2018.
- 692 ECMWF-IFS. Part IV: PHYSICAL PROCESSES(CY33R1). Technical Report, 2008.
- 693 Ettema J, van den Broeke M. R., E. van Meijgaard, and W. J. van de Berg. 2010. Climate of the
694 Greenland ice sheet using a high-resolution climate model-Part 2: Near-surface climate and
695 energy balance. *The Cryosphere*, 4, 529-544, 2010.
- 696 Fang Z F. Statistical relationship between the northern hemisphere sea ice and atmospheric
697 circulation during winter time. In *Observation, Theory and Modeling of Atmospheric Variability*.
698 World Scientific Series on Meteorology of East Asia, Zhu X (ed). World Scientific Publishing
699 Company: Singapore, 131-141, 2004.
- 700 Fausto, R.S., Van As, D., Box, J. E., Colgan, W., Langen, P. L.: Quantifying the Surface Energy
701 Fluxes in South Greenland during the 2012 High Melt Episodes Using In situ Observations. *Front.*
702 *Earth Sci.* 4:82. doi: 10.3389/feart.2016.00082, 2016.
- 703 Fausto, R.S., Van As, D., Ahlstrøm, A.P., Citterio, M.: Instruments and Methods Assessing the
704 accuracy of Greenland ice sheet ice ablation measurements by pressure transducer. *J. Glaciol.*,
705 Vol. 58, No. 212, 2012. doi: 10.3189/2012JoG12J075, 2012b.
- 706 Fausto, R.S., Van As, D., Ahlstrøm, A.P., Andersen, S.B., Andersen, M.L., Citterio, M., et al.: Ablation
707 observations for 2008-2011 from the Programme for Monitoring of the Greenland Ice Sheet
708 (PROMICE). *Geolo. Surv. Den. Greenl. Bull.* 26, 25-28, 2012a.
- 709 Greuell, W. and Konzelman, T.: Numerical modelling of the energy balance and the englacial
710 temperature of the Greenland ice sheet. Calculations for the ETH-Camp location (West
711 Greenland, 1155 m a.s.l.), *Global Planet. Change.*, 9, 91-114, [https://doi.org/10.1016/0921-8181](https://doi.org/10.1016/0921-8181(94)90010-8)
712 (94) 90010-8, 1994.
- 713 Hanna E, Cappelen J.: Recent cooling in coastal southern Greenland and relation with the North
714 Atlantic Oscillation. *Geophys. Res. Lett.*, 30:1132, DOI: 10.1029/2002GL015797, 2003.
- 715 Hanna E, Cropper TE, Hall RJ and Cappelen J.: Greenland blocking index 1851-2015: a regional
716 climate change signal. *Int. J. Climatol.*, 36, 4847-4861 (doi: 10.1002/joc.4673), 2016.
- 717 Hanna E, Cropper TE, Hall RJ, Scaife AA and Allen R.: Recent seasonal asymmetric changes in
718 the NAO (a marked summer decline and increased winter variability) and associated changes in
719 the AO and Greenland blocking index. *Int. J. Climatol.*, 35, 2540-2554. doi: 10.1002/joc.4157,
720 2015.
- 721 Hanna E, Jones JM, Cappelen J, Mernild SH, Wood L, Steffen K, Huybrechts P.: The influence of
722 North Atlantic atmospheric and oceanic forcing effects on 1900-2010 Greenland summer climate
723 and ice melt/runoff. *Int. J. Climatol.* 33: 862-880, doi: 10.1002/joc.3475, 2013.
- 724 Hanna, E., X. Fettweis, S.H. Mernild, J. Cappelen, M.H. Ribergaard, C.A. Shuman, K. Steffen, L.
725 Wood, T.L. Mote.: Atmospheric and oceanic climate forcing of the exceptional Greenland ice
726 sheet surface melt in summer 2012. *Int. J. Climatol.* 34, 1022-1037, 2014.
- 727 Hersbach, H. and Dee, D.: "ERA-5 reanalysis is in production", ECMWF newsletter, 147, 7, 2016.
- 728 Hoch, S. W., Calanca, P., Philipona, R., and Ohmura, A.: Year round observation of longwave
729 radiative flux divergence in Greenland, *J. Appl. Meteorol.*, 46, 1469-1479, doi:10.1175/JAM
730 2542.1, 2007.



- 731 Hofer, S., A.J. Tedstone, X. Fettweis, J.L. Bamber.: Decreasing cloud cover drives the recent mass
732 loss on the Greenland ice sheet. *Science Advances.*, 3, e1700584, 2017.
- 733 Holtslag, A. and de Bruin, H.: Applied modeling of the nighttime surface energy balance over land,
734 *J. Appl. Meteorol.*, 27, 689-704, 1988.
- 735 Hurrell J and National Center for Atmospheric Research Staff (eds).: *The Climate Data Guide:*
736 *Hurrell North Atlantic Oscillation (NAO) Index (PC-based)*. Retrieved from
737 <https://climatedataguide.ucar.edu/guidance/hurrell-north-atlantic-oscillation-nao-index-pc-based>,
738 2012.
- 739 Hurrell JW, Kushnir Y, Ottersen G, Visbeck M (eds).: *The North Atlantic Oscillation: Climatic*
740 *Significance and Environmental Impact*. American Geophysical Union: Washington, DC, 279 pp.
741 2003.
- 742 Hurrell JW. Decadal trends in the North Atlantic oscillation: regional temperatures and
743 precipitation. *Science.*, 269: 676-679. 1995.
- 744 IPCC.: *Special Report on the Ocean and Cryosphere in a Changing Climate* Intergovernmental
745 Panel on Climate Change, Special Report on the Oceans and Cryosphere in a changing climate,
746 2019.
- 747 Jones PD, Osborn TJ, KE B. Pressure based measures of the North Atlantic Oscillation (NAO): A
748 comparison and an assessment of changes in the strength of the NAO and in its influence on
749 surface climate parameters. In *The North Atlantic Oscillation: Climatic Significance and*
750 *Environmental Impact (Geophysical Monograph)*, Hurrell JW, Kushnir Y, Ottersen G, Visbeck
751 M (eds). American Geophysical Union: Washington, DC, 51-62. 2003.
- 752 Khan, S. A., A. Aschwanden, A. A. Bjørk, J. Wahr, K. K. Kjeldsen, and K. H. Kjær.: Greenland ice
753 sheet mass balance: A review, *Rep. Prog. Phys.*, 78(4), 046801, doi:10.1088/0034-4885/78/4/0
754 46801, 2015.
- 755 Kuipers Munneke, P. C. J. P. P. Smeets, C. H. Reijmer, J. Oerlemans, R. S. W. van de Wal and M.
756 R. van den Broeke.: *The K-transect on the western Greenland Ice Sheet: Surface energy balance*
757 (2003-2016), *Arct. Antarct. Alp.*, 50:1, e1420952, DOI:10.1080/15230430.2017.1420952, 2018.
- 758 Kuipers Munneke, P., M. R. van den Broeke, C. H. Reijmer, M. M. Helsen, W. Boot, M.
759 Schneebeli, and K. Steffen.: *The role of radiation penetration in the energy budget of the*
760 *snowpack at Summit, Greenland*. *The Cryosphere.*, 3:155-65. doi:10.5194/tc-3155-2009, 2009.
- 761 Kuipers Munneke, P., van den Broeke, M. R., King, J. C., Gray, T., and Reijmer, C.H.: Near
762 -surface climate and surface energy budget of Larsen C ice shelf, Antarctic Peninsula, *The*
763 *Cryosphere*, 6, 353-363, <https://doi.org/10.5194/tc-6-353-2012>, 2012.
- 764 Nghiem, S. V., D. K. Hall, T. L. Mote, M. Tedesco, M. R. Albert, K. Keegan, C. A. Shuman, N. E.
765 Di Girolamo, and G. Neumann.: *The extreme melt across the Greenland ice sheet in 2012*.
766 *Geophys. Res. Lett.*, 39: L20502. doi:10.1029/2012GL053611, 2012.
- 767 Nođ, B., van de Berg, W. J., van Meijgaard, E., van de Wal, R. S. W., and van den Broeke, M. R.:
768 *Modelling the climate and surface mass balance of polar ice sheets using RACMO2-Part1:*
769 *Greenland (1958-2016)*, *The Cryosphere*, 12, 811-831, <https://doi.org/10.5194/tc-12-811-2018>,
770 2018.
- 771 Nođ, B., W. J. van de Berg, S. Lhermitte, M. R. van den Broeke, *Rapid ablation zone expansion*
772 *amplifies north Greenland mass loss*. *Sci. Adv.* 5, eaaw0123, 2019.
- 773 Oerlemans, J. and Vugts, H. F.: *A Meteorological experiment in the melting zone of the Greenland*
774 *ice sheet*, *B. Am. Meteorol. Soc.*, 74, 3-26, 1993.



- 775 Overland J E, Francis J A, Hanna E, et al. The recent shift in early summer Arctic atmospheric
776 circulation. *Geophys. Res. Lett.*, 39 (19): 19804, doi: 10.1029/2012GL053268. 2012.
- 777 Overland J E, Wang M. Large-scale atmospheric circulation changes are associated with the recent
778 loss of Arctic sea ice. *Tellus A*, 62 (1): 1-9, 2010.
- 779 Rajewicz, J., and S. J.: Marshall Variability and trends in anticyclonic circulation over the
780 Greenland ice sheet, 1948-2013, *Geophys. Res. Lett.*, 41, 2842-2850, doi: 10.1002/2014GL
781 059255, 2014.
- 782 Reijmer, C. and Hock, R.: Internal accumulation on Storglaciären, Sweden, in a multi-layer snow
783 model coupled to a distributed energy-and mass-balance model, *J. Glaciol.*, 54, 61-72, <https://doi.org/10.3189/002214308784409161>, 2008.
- 784
785 Reijmer, C. H. and Oerlemans, J.: Temporal and spatial variability of the surface energy balance in
786 Dronning Maud Land, East Antarctica, *J. Geophys. Res.*, 107, 4759, <https://doi.org/10.1029/2000JD000110>, 2002.
- 787
788 Rimbu N. and Lohmann G. : Winter and summer blocking variability in the North Atlantic region
789 - evidence from long-term observational and proxy data from southwestern Greenland. *Clim.
790 Past*, 7, 543-555, 2011.
- 791 Shepherd, A., Ivins, E., Rignot, E. et al. Mass balance of the Greenland Ice Sheet from 1992 to
792 2018. *Nature*, doi:10.1038/s41586-019-1855-2, 2019.
- 793 Smeets, C. J. P. P. and Van den Broeke, M. R.: Parameterizing scalar roughness over smooth and
794 rough ice surfaces, *Bound. Lay. Meteorol.*, 128, 339-355, 2008.
- 795 Smeets, Paul C. J. P., Peter Kuipers Munneke, Dirk van As, Michiel R. van den Broeke, Wim Boot,
796 Hans Oerlemans, Henk Snellen, Carleen H. Reijmer and Roderik S. W. van de Wal.: The
797 K-transect in west Greenland: Automatic weather station data (1993-2016), *Arct. Antarct. Alp.*,
798 50:1, S100002, DOI: 10.1080/15230430.2017.1420954, 2018.
- 799 Steffen, K. and Box, J.E.: Surface climatology of the Greenland ice sheet: Greenland climate
800 network 1995-1999. *J. Geophys. Res.*, 106(D24), 33,951-33,964. 2001.
- 801 Steffen, K., J. Box and W. Abdalati.: Greenland climate network: GC-net. *CRREL Spec. Rep.*
802 96-27, 98-103. 1996.
- 803 Van As D., Fausto RS and PROMICE Project Team.: Programme for monitoring of the Greenland
804 Ice Sheet (PROMICE): first temperature and ablation records. In Bennike O, Garde AA and Watt
805 WS eds. Review of survey activities 2010. GEUS, Copenhagen, 73-76 (*Geological Survey of
806 Denmark and Greenland Bulletin*, 23. 2011).
- 807 Van As D., Hubbard A. L., B. Hasholt, A. B. Mikkelsen, M. R. van den Broeke, and R. S. Fausto.
808 Large surface meltwater discharge from the Kangerlussuaq sector of the Greenland ice sheet
809 during the record-warm year 2010 explained by detailed energy balance observations *The
810 Cryosphere*, 6, 199-209, 2012.
- 811 Van den Broeke, M. R., C. J. P. P. Smeets, and R. S. W. van de Wal.: The seasonal cycle and
812 interannual variability of surface energy balance and melt in the ablation zone of the west
813 Greenland ice sheet. *The Cryosphere.*, 5:377-90. doi:10.5194/tc-5-377-2011. 2011.
- 814 Van den Broeke, M. R., D. van As, C. H. Reijmer, and R. S. W. van de Wal.: Sensible heat
815 exchange at the Antarctic snow surface: A study with automatic weather stations. *International
816 Journal of Climatology*, 25:1080-101. doi:10.1002/joc.1152. 2005.
- 817 Van den Broeke, M. R., J. Box, X. Fettweis, E. Hanna, B. Noč, M. Tedesco, D. van As, W. J. van
818 de Berg and L. van Kampenhout.: Greenland ice sheet surface mass loss: recent developments in



- 819 observation and modelling. *Current Climate Change Reports*, doi.org/10.1007/s40641-017-0084-
820 8, 2017.
- 821 Van den Broeke, M. R., Reijmer C. H., Van d. W. R. S. W.: A study of the surface mass balance in
822 Dronning Maud Land, Antarctica, using automatic weather stations. *J. Glaciol.*, 50(171),
823 565-582. 2004.
- 824 Van den Broeke, M. R.: Characteristics of the lower ablation zone of the west Greenland ice sheet
825 for energy-balance modelling, *Ann. Glaciol.*, 23, 160-166, 1996.
- 826 Van den Broeke, M., P. Smeets and J. Ettema.: Surface layer climate and turbulent exchange in the
827 ablation zone of the west Greenland ice sheet. *Int. J. Climatol.*, 29(15), 2309-2323. 2009.
- 828 Van den Broeke, M., P. Smeets, J. Ettema, and P. K. Munneke.: Surface radiation balance in the
829 ablation zone of the west Greenland ice sheet, *J. Geophys. Res.*, 113, D13105, doi:10.1029/
830 2007JD009283. 2008a.
- 831 Van den Broeke, M., Smeets, P., Ettema, J., van der Veen, C., van de Wal, R., and Oerlemans, J.:
832 Partitioning of melt energy and meltwater fluxes in the ablation zone of the west Greenland ice
833 sheet, *The Cryosphere*, 2, 179-189, 2008b.
- 834 Van Meijgaard, E., van Ulft, L. H., van de Berg, W. J., Bosveld, F. C., van den Hurk, B. J. J. M.,
835 Lenderink, G., and Siebesma, A. P.: The KNMI regional atmospheric climate model RACMO
836 version 2.1, Tech. Rep. 302, KNMI, De Bilt, The Netherlands, 2008.
- 837 Young-Kwon Lim et al.: Atmospheric summer teleconnections and Greenland Ice Sheet surface
838 mass variations: insights from MERRA-2. *Environ. Res. Lett.* 11 024002, 2016.